Nanoscale Geometric Electric Field Enhancement in Organic Photovoltaics

Lara-Jane Pegg and Ross A. Hatton*

Department of Chemistry, University of Warwick, Coventry, England, CV4 7AL

ABSTRACT

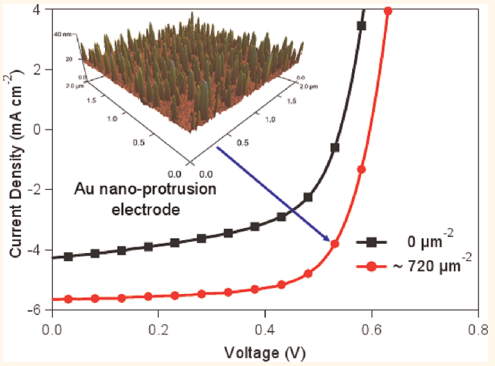

Generic design rules for electrode—organic semiconductor contacts that transcend specific materials are urgently required to guide the development of new electrodes and provide a framework for engineering this important class of interface. Herein a novel nanostructured window electrode is utilized in conjunction with three-dimensional electrostatic modeling to elucidate the importance of geometric electric field enhancement effects at the electrode interfaces in organic photovoltaics. The results of this study show that nanoscale protrusions at the electrode surfaces in organic photovoltaics dramatically improve the efficiency of photogenerated charge carrier extraction to the external circuit and that the origin of this improvement is the local amplification of the electrostatic field in the vicinity of said protrusions. This wholly geometric approach to engineering electrodes at the nanoscale is materials generic and can be employed to enhance the efficiency of charge carrier injection or extraction in a wide range of organic electronic devices.

KEYWORDS: organic photovoltaics · geometric electric field enhancement · electrode · bulk heterojunction · nanoprotrusion

Organic photovoltaics (OPVs) have strong potential as a low-cost route to sustainably harvesting electricity directly from sunlight, particularly for the provision of off-grid electricity[1−3] and portable consumer electronics.[4] In this class of photovoltaic device the electrode—organic semiconductor interfaces are critical determinants of both the efficiency with which light is converted to electricity and the operational lifetime. It is therefore imperative that these interfaces are engineered to be robust toward large fluctuations in temperature and light intensity while minimizing energy losses incurred when extracting charges to the external circuit. In recent years a number of innovative electrode and charge carrier extraction materials for OPVs have been proposed including several based on nanomaterials.[5−8] However, current understanding of the correlation between device performance and the detailed nanostructure at the electrode interfaces is at an early stage of development.[8−14] Unlike interfacial barriers at metal—inorganic semiconductor contacts, which are largely insensitive to the initial Fermi level of the electrode, the interfacial energetics at metal—organic semiconductor interfaces are much more difficult to predict.[15,16] Consequently, there is a clear need for the elucidation of generic design rules that transcend specific materials systems to guide the development of new electrodes and provide a framework for engineering this important class of interface.

The most powerful causes of photovoltaic action in an OPV are the heterojunction between the donor and acceptor materials and the built-in electric field, both of which operate to break the symmetry of the photoactive layer. In the most efficient single-junction OPV systems to date the donor and acceptor phases have a bulk-heterojunction (BHJ) architecture, which is characterized by a complex interpenetrating network of the two phases.[1,2,4,11] One consequence of this morphology is that a large built-in electric field is required to break device symmetry, and so a major cause of energy loss is the erosion of the charge carrier collection efficiency close to the open-circuit condition (V_{oc}) due to the recombination of electrons and holes.[17,18] Furthermore, Jeong *et al.*[19] have recently shown that this voltage-dependent effect is amplified when the device area is scaled for applications. Strategies to increase the built-in electric field strength in this important class of OPV therefore offer a path to maximizing device power conversion efficiency (η).

* Address correspondence to ross.hatton@warwick.ac.uk.

Received for review November 24, 2011 and accepted May 10, 2012.

Published online May 10, 2012
10.1021/nn3007042

Herein we show that geometric electric field enhancement (GEFE) in the vicinity of nanoscale protrusions at the substrate electrode surface in BHJ OPVs can be harnessed to increase device η by enhancing the efficiency of charge carrier collection. The power of this wholly geometric approach to electrode design is threefold: (i) it can be applied to any electrode whose surface can be decorated with nanoscale protrusions and is thus materials generic; (ii) it can be employed to facilitate charge carrier injection or extraction, rendering it useful for a range of organic electronic applications beyond photovoltaics, including light-emitting diodes and transistors; (iii) electrode selectivity for the injection or extraction of a specific charge carrier type is enhanced, reducing electrical losses and simplifying device architecture by removing the need for additional blocking layers. While the possibility that this phenomenon plays a role in the operation of organic optoelectronic devices has previously been proposed in the context of carbon nanotube electrodes,[20,21] convincing evidence to support this hypothesis has been lacking due to the difficulty in separating GEFE effects from other factors known to be critical determinants of charge carrier transport across organic semiconductor−electrode interfaces. For example, by changing the electrode topography using carbon nanotubes, the work function (φ), surface energy (γ), chemical makeup, and electrical conductivity of the electrode are all simultaneously altered. The energetics and morphology at electrode−organic semiconductor interfaces are complex functions of all of these surface parameters,[10−16,22] and so it is not possible to isolate the effect of the change in topography. From a practical perspective the surface roughness of most commercially available substrate electrodes, including ITO glass,[23] is too high to be suitable for investigating the impact of nanoscale protrusions at the electrode.

To demonstrate the operation of GEFE in OPVs, we have developed a window electrode that is exceptionally smooth and can be decorated with a controllable density of nanoscale protrusions of well-defined geometry. The electrode is designed such that the incorporation of protrusions at its surface does not perturb φ, γ, or the chemical composition, and so it can be assumed that the energetics at the interface with any given organic semiconductor are common to the contacts with and without protrusions. These model electrodes also enable direct correlation between experimental measurements and the results of three-dimensional electrostatic simulations in which only the system geometry is considered. Upon incorporation into model BHJ OPVs, the current−voltage (J−V) characteristics in the dark, under 1 sun simulated solar illumination and as a function of the protrusion surface density, all exhibit evidence of GEFE effects and demonstrate the power of this wholly geometric approach to electrode engineering.

The phenomenon of GEFE[24] is exploited in applications where cold electron sources are required and the electrons are injected into vacuum, including field-emission displays and electron microscopes. In electrode configurations resembling a parallel plate capacitor the bulk electric field (F_{bulk}) is given by V/d, where d is the electrode separation and V is the potential difference between the electrodes. The electric field very close to the surface of the electrodes, F_{local}, can however be many times higher than F_{bulk} at the site of microscopic protrusions on the electrode surface due to the concentration of the lines of equipotential around the protrusion apex.[25−27] Since it is the electric field strength within a few nanometers of the emitting surface that controls the barrier to electron emission *via* tunneling, it is F_{local} rather than F_{bulk} that determines the onset of field emission from a surface protrusion. When the density of protrusions at the electrode surface is sufficiently high, the total field emission current from the electrode is dominated by that from the protrusions, and the J−V characteristic can be expressed by the simplified Fowler−Nordheim equation:[28]

$$J = aF^2 e^{-\left(\frac{\kappa}{\beta F}\right)}$$

where J is the current density, $F = F_{bulk}$, a and κ are constants, and β is defined as the ratio F_{local}:F_{bulk}. According to this well-established model, a plot of $\ln(J/F^2)$ *vs* $1/F$ is linear and, to a good approximation, β can be extracted directly from the gradient of the graph in the high-field region.[24−27] However, in the context of the reverse process of charge carrier extraction the magnitude and extent of F enhancement at distances greater than a few nanometers from the protrusion surface is also of critical importance.

Figure 1 summarizes the results of three-dimensional electrostatic simulations of F between parallel plate electrodes, one of which has an isolated conducting protrusion at its surface. In this configuration the electrode planes are separated by 220 nm and the surface protrusion has an idealized *hemisphere-on-a-post* geometry[24] with a height and radius of 13.6 and 7.5 nm, respectively. This geometry corresponds to the dimensions of the conducting protrusions realized experimentally herein. Likewise the electrode separation corresponds to that of hole-only diodes fabricated as part of this study and is typical of prototypical BHJ OPVs based on a poly(3-hexylthiophene) (P3HT):[6,6]-phenyl-C_{61}-butyric acid methyl ester (PCBM) blend.[29] In Figure 1a−c the Au electrode is biased by +0.1 V, although it is important to emphasize that the relative enhancement in F is independent of the magnitude or polarity of F_{bulk}.[24−27] It is evident from Figure 1a that for the geometry simulated F decays exponentially to F_{bulk} over a distance of ~50 nm from the protrusion apex along the axis normal to the electrode, and so the

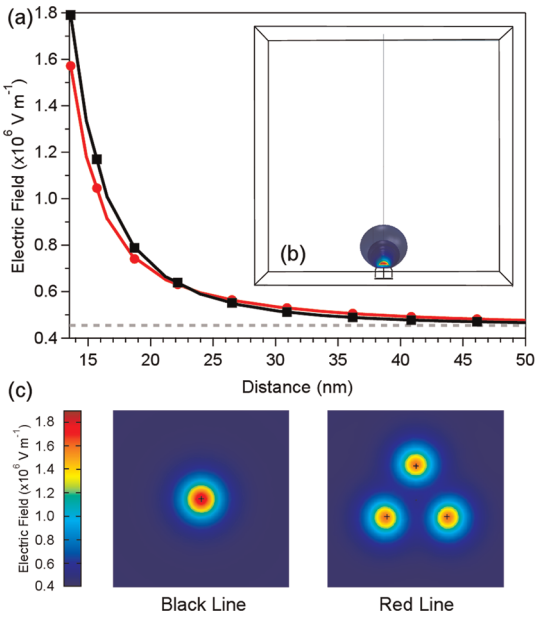

Figure 1. (a) Three-dimensional electrostatic simulation (COMSOL Multiphysics) of the change in *F* with distance from the apex of an isolated nanoscale protrusion (black line) with a hemisphere-on-a-post geometry. The radius and height of the protrusion is 7.5 and 13.6 nm, respectively, and the separation between the planes of the substrate electrode and the counter electrode is 220 nm, which corresponds to the geometry realized experimentally. The simulation work space is 220 nm × 220 nm × 220 nm. The potential difference across the electrodes is chosen to be +0.1 V. To illustrate the effect of *F* screening by adjacent protrusions, the variation in *F* with distance from the apex of a protrusion in close proximity to two others is also shown (red line). The protrusion separation is 1.5 nm. The dashed gray line corresponds to $F_{bulk} \approx 0.45 \times 10^6$ V m^{-1}. (b) Three-dimensional representation of the sphere of influence above an isolated nanoscale protrusion to within 99% of F_{bulk}. Simulation performed in a 220 nm × 220 nm × 220 work space. (c) Variation in *F* in a plane 13.6 nm above the plane of the substrate that intersects the apex of the protrusions simulated.

increase in *F* results from GEFE rather than the reduced distance between the tip of the protrusion and the counter electrode.[26] Figure 1b depicts the volume immediately above the protrusion over which *F* is enhanced as compare to F_{bulk}. The region of enhanced *F* is approximately spherical, enabling the protrusion to extract photogenerated charge carriers formed in parts of the photoactive material that are not immediately above it. This increase in *F* facilitates hole extraction to the external circuit, while simultaneously inhibiting electron extraction by increasing the potential barrier to electron extraction. One characteristic of GEFE effects is the sensitivity of β to the proximity of adjacent protrusions. Two-dimensional electrostatic simulations of carbon nanotube arrays by Nilsson *et al.* predict that the onset of field screening begins for protrusion separations approximately twice the protrusion height.[30] On the basis of this rule-of-thumb, the optimal density of protrusions in the current context is ~600 μm^{-2}. To illustrate the impact of *F* screening on β, the results of a simulation pertaining to the specific case where three protrusions are in very close proximity are shown in Figure 1a, c (right). It is evident that the adverse impact of clustering is threefold: (i) β is reduced; (ii) the surface area of the protrusion apex over which *F* is enhanced is reduced; (iii) in the direction normal to the plane of the electrodes *F* converges to F_{bulk} more rapidly. For these reasons it is important that protrusion clustering is avoided and the surface density is carefully controlled.

A chemically well-defined, highly transparent, and exceptionally smooth model electrode was fabricated by evaporating 9 nm of Au onto a glass substrate derivatized with a monolayer of the molecular adhesive 3-mercaptopropyltrimethoxysilane (MPTMS). The molecular adhesive binds to the glass substrate *via* strong siloxane linkages and immobilizes incident Au atoms upon arrival, which react with the thiol moieties, thereby promoting continuous film formation at low thickness.[31−34] These ultrathin films have a mean absolute transparency of 63% across the visible spectrum (400−750 nm) (Figure S1, Supporting Information) and an exceptionally low root-mean-square roughness (~0.6 nm), making them ideally suited as a *model* window electrode for the purpose of this study. To realize an array of surface protrusions with a tight size distribution and maximum height suitable for incorporation into an OPV device, MPTMS-derivatized glass substrates were decorated with a random array of 12.5 ± 1.2 nm oleylamine (OAm)-capped Au nanoparticles. The surface density of nanoparticles is controlled by varying the time the MPTMS-derivatized substrate is submerged in the nanoparticle solution. To render the surface of the nanoparticles *sticky* toward incoming Au atoms, the OAm ligand was exchanged with 1,5-pentanedithiol, as illustrated in Figure 2b. Nine nanometers of Au was then thermally evaporated onto the nanoparticle-decorated glass substrate to form a 9 nm Au film with a random array of 13.6 ± 2.9 nm tall surface protrusions (Figure 2c). The sheet resistance of these electrodes is marginally increased upon incorporation of protrusions from 13.6 ± 0.6 Ω sq^{-1} to 16.9 ± 1.8 Ω sq^{-1}, although this is not sufficient to significantly impact the performance of 6 mm^2 diodes fabricated on 1.44 cm^2 substrates. The absolute transparency of the 9 nm Au films was reduced by <5% upon incorporation of protrusions (Figure S1, Supporting Information). Immediately prior to device fabrication the substrates were UV/O_3 treated to oxidize the surface to a depth of ~1 nm, which raises the φ to ~5.4 eV while remaining sufficiently thin to be transparent to electron transport across the interface.[8,35] Importantly, surface potential measurements made using an atomic force microscope (AFM) confirm that the protrusions have the same φ to within 15 meV as the surrounding flat area (Figure S2, Supporting Information). The surface energy of freshly UV/O_3-treated substrates with and without nanoprotrusions was measured to be

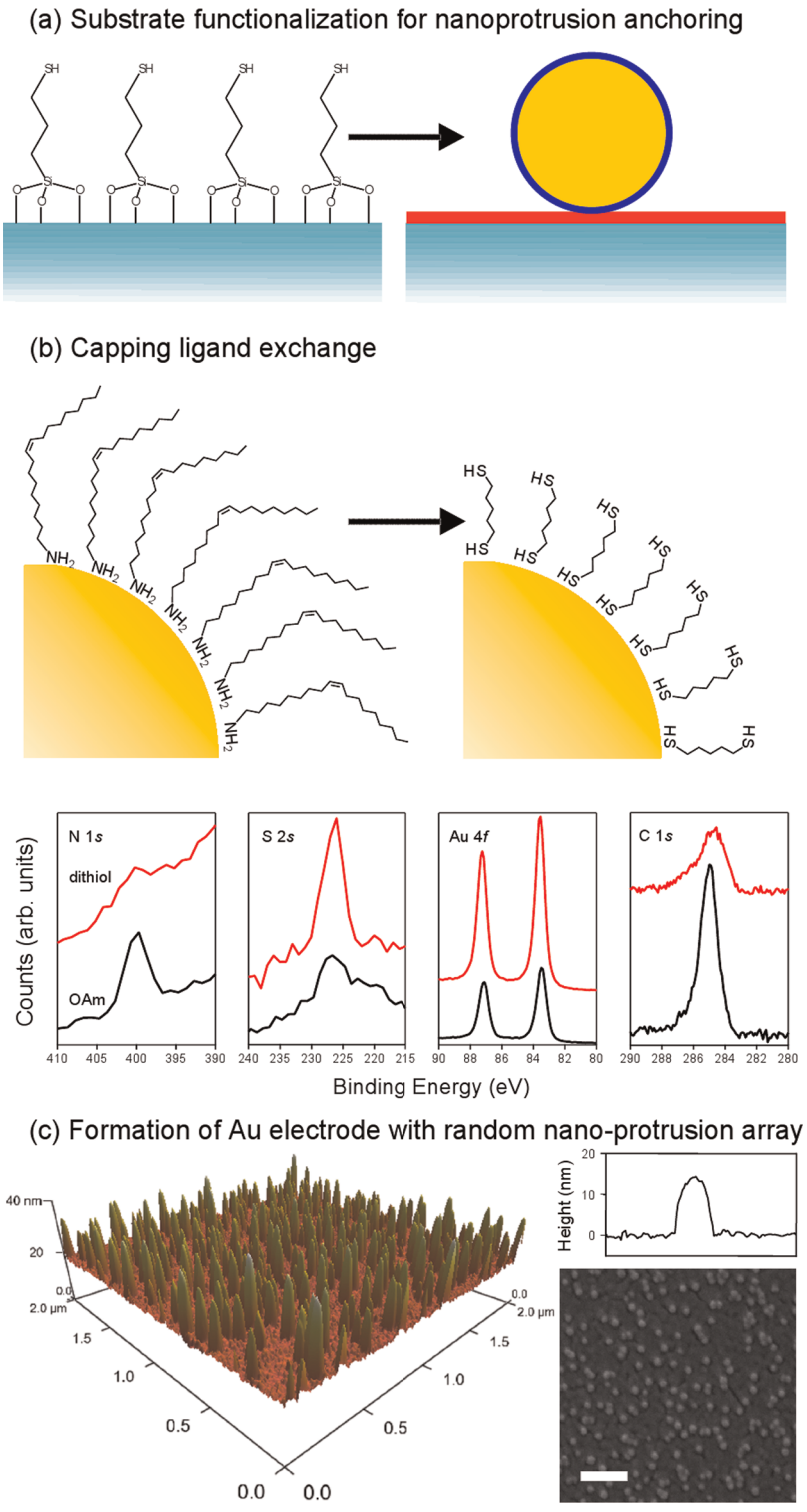

Figure 2. Step-by-step fabrication of ultrasmooth Au electrodes with a random array of nanoscale protrusions. (a) Functionalization of a glass substrate with an MPTMS monolayer (left) onto which OAm-capped Au nanoparticles are immobilized. The size distribution measured using a TEM of the OAm-capped nanoparticles is 12.5 ± 1.2 nm. (b) The OAm ligand is exchanged with 1,5-pentanedithiol to render the surface *sticky* toward incoming Au atoms. The high efficiency of this exchange reaction was verified using X-ray photoelectron spectroscopy. The loss of the N 1s signal intensity and large decrease in the C 1s signal in conjunction with an increase in the S 2s and Au 4f signals is consistent with the substitution of the long alkyl chain and buried amine headgroup of the OAm capping ligand with the much shorter 1,5-pentanedithiol ligand. The S 2s signal from the OAm-capped nanoparticles prior to ligand exchange derives from the MPTMS monolayer at the glass surface. (c) 9 nm of Au was thermally evaporated onto a glass substrate decorated with nanoparticles, resulting in a random array of nanoscale protrusions on the electrode surface (3D AFM image, left, and FE-SEM image, right; scale bar 100 nm). The protrusion heights and widths were measured using an AFM and FE-SEM, respectively.

73.3 ± 0.2 and 73.1 ± 0.2 mJ m^{-2}, respectively. In short these model electrodes are essentially identical in chemical composition, φ and γ, allowing the impact of GEFE effects to be isolated.

Field emission scanning electron microscopy (FE-SEM) images of substrates decorated with nanoscale protrusions confirm that electron emission is most efficient from protrusions (Figure 2c). To test the validity of the electrostatic modeling, hole-only diodes based on the archetypal organic semiconductor P3HT were fabricated using Al as the counter electrode. In these diodes the barrier to hole injection from the Fermi level of the Au electrode into the highest occupied molecular orbital (HOMO) of P3HT is small (~0.1 eV),[35] due to the high φ of surface-oxidized Au. Conversely the barrier to electron injection from the Al Fermi level (~4.3 eV below the vacuum level)[36] into the lowest unoccupied molecular orbital (LUMO) of P3HT (~2.7 eV below the vacuum level)[37] is expected to be prohibitively large (≫1 eV).[38] A consequence of this asymmetry in the barrier heights to electron and hole injection is that the measured current is dominated by the hole current injected from the Au electrode.[38,39] To corroborate this assumption, the Al electrode in reference diodes was substituted with Au, which has a much higher φ, ~5.1 eV[36] *vs* ~4.3 eV,[36] in order to further increase the barrier to electron injection. The measured current under forward bias was found to be unchanged (Supporting Information, S3), supporting the assumption that the barrier to electron injection in diodes employing both Al and Au as cathode materials is sufficiently high to prevent significant electron injection over the range of F strengths investigated. Furthermore, in this study all diodes were fabricated and tested in a dry nitrogen atmosphere without exposure to the laboratory environment, since it is known that P3HT forms a Schottky contact with Al upon exposure to ambient air due to p-type doping of the P3HT.[40] When P3HT diodes employing an Al electrode are fabricated and tested in the absence of air, it can be assumed that the p-type doping density is sufficiently low that, to a good approximation, the electric field across the P3HT layer is uniform and the metal–insulator–metal model is applicable.[38] To test this assumption, the φ of P3HT films prepared under nitrogen was measured using a Kelvin probe (also in a nitrogen atmosphere) without exposure to the laboratory environment. The measured φ, 4.28 ± 0.02 eV, is essentially identical to that of the Al electrode (4.28 eV),[36] and so there is no thermodynamic driver for Schottky contact formation. Furthermore, the maximum hole current that can pass through the P3HT layer is limited by space charge and is achieved when the hole-injecting contact is ohmic.[41] When F across the semiconductor layer is uniform, the space charge limited current is given by the Mott–Gurney law,[42] which predicts that $J^{0.5}$ is proportional to V provided

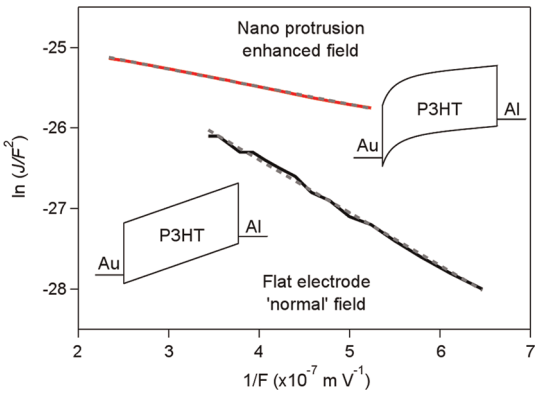

Figure 3. Representative Fowler–Nordheim plots for P3HT hole-only diodes employing Au electrodes with ~720 nanoscale protrusions μm^{-2} (red) and without protrusions (black). The P3HT thickness was 220 nm. Only the high-field regime is shown.

the charge carrier mobility is independent of electric field strength, as is known to be the case for highly crystalline P3HT over the range of electric field strengths used in this study.[38] The linearity of the graph of $J^{0.5}$ *vs* V (Supporting Information, Figure S3 (inset)) is consistent with the expectation that the barrier to hole injection is sufficiently small to be ohmic and that the electric field falls uniformly across the P3HT layer. When the barrier to hole injection is small, holes tunnel directly from the Au/AuO_x electrode Fermi level into the HOMO of the P3HT according to the Fowler–Nordheim equation.[28] The linearity of the ln(J/F^2) *vs* 1/F plots in the high-F regime for diodes with and without protrusions at the surface of the Au electrode indicates that the emission mechanism is consistent with Fowler–Nordheim tunneling injection (Figure 3). From the gradient and intercept of the plots associated with the reference electrode, the prefactor a and exponent κ can be extracted. These constants embody a number of physical parameters that are common to electrodes with and without protrusions including the effective mass of holes in P3HT, corrections to account for the relatively low charge carrier mobility and random energetic barriers caused by disorder in organic semiconductors and the oxide layer thickness.[43,44] Using these constants in conjunction with β determined by electrostatic simulation on the basis of protrusion geometry alone, the calculated J–V characteristic for the electrode with protrusions is shown in Figure 4. The protrusion density was assumed to be the average achieved experimentally: ~720 μm^{-2}. The emission current is weighted by the fraction of the total area with and without protrusions. The model accounts for the variation of β across the surface of each protrusion (Figure 4, inset) and in the area between protrusions as predicted by the simulation (Supporting Information, S4 and Table S.1). Since it is the magnitude of F within 1–2 nm of the electrode surface that controls charge carrier injection

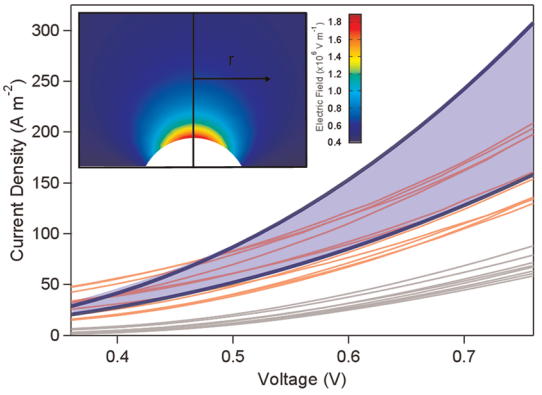

Figure 4. *J*–*V* characteristics for hole-only P3HT diodes based on Au electrodes with ~720 protrusions μm^{-2} (red curves) and without protrusions (gray curves). The blue lines represent the *J*–*V* characteristics calculated according to the simplified Fowler–Nordheim equation using β values derived from the 3D electrostatic simulation and the range of κ and *a* extracted from the Fowler–Nordheim plots for diodes employing electrodes *without* protrusions. Details of the calculation are given in the Supporting Information.

via field-assisted tunneling, it is β at the electrode surface that is the relevant β parameter in this context. Details of this calculation are provided in the Supporting Information. The excellent agreement between the experimental data and the calculated *J*–*V* characteristic provides compelling evidence that the origin of the increase in *J* is local amplification of *F* in the vicinity of the protrusions. The modest divergence with increasing *F* stems from the assumption in the model that the maximum β value is always achieved. It is evident from Figure 2c that in practice a significant proportion of nanoprotrusions are in close proximity to one another, which operates to reduce β (Figure 1c), and so the model fractionally overestimates the gradient of the *J*/*V* characteristic.

Having demonstrated that the experimental measurements of hole injection in unipolar diodes can be rationalized in terms of wholly geometric considerations, the possibility that GEFE effects might be harnessed to improve the efficiency of the reverse process of hole extraction in the context of BHJ OPVs was investigated. For this purpose prototypical BHJ OPVs were fabricated using a 1:1 blend of the electron acceptor PCBM and electron donor P3HT. The photoactive layer was deposited from a slowly dried 40 mg mL^{-1} 1,2-dichlorobenzene solution, yielding a total film thickness of 270 nm. In the first instance the number density of protrusions was chosen to be as high as possible without significant aggregation (~720 μm^{-2}) and is close to the optimal number density predicted by Nilsson *et al.*[30] for carbon nanotube electron field emitters. To check that the incorporation of protrusions at the electrode surface does not significantly perturb the blend microstructure in the critical region close to the substrate electrode, thin P3HT:PCBM films were prepared from a 5 mg mL^{-1} solution and probed using AFM and electronic absorption spectroscopy.

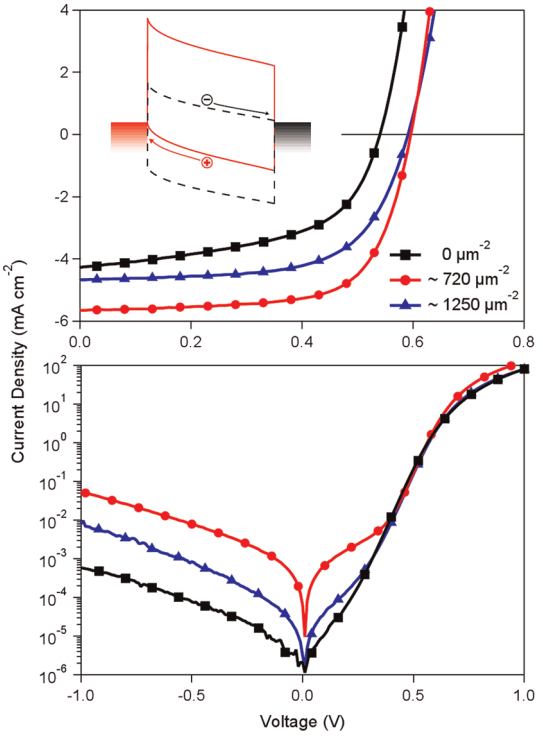

Figure 5. *J*–*V* characteristics for P3HT:PCBM OPVs employing model Au window electrodes with different densities of nanoscale surface protrusions: 0 μm^{-2} (black squares); ~720 μm^{-2} (red circles); ~1250 μm^{-2} (blue triangles). Device characteristics were measured under 1 sun simulated solar illumination (100 mW cm^{-2}) (top) and in the dark (bottom). Top (inset) Schematic energy level diagram illustrating the effect of GEFE on the frontier orbital energies of P3HT (red continuous line) and PCBM (dotted black line).

The comparable topography of the surface of these thin films confirms that the protrusions are embedded in the organic overlayer (Figure S5, Supporting Information). Electronic absorption spectroscopy is a sensitive probe of differences in the morphology and microstructure of P3HT and PCBM films,[45–48] and so the absence of any significant difference in the absorption spectrum is evidence that the microstructure of the P3HT:PCBM film in the region close to the interface is essentially unchanged (Figure S6 Supporting Information). Upon incorporation of protrusions at the electrode interface, short-circuit current density (J_{sc}), V_{oc}, and fill factor (FF) are all significantly enhanced (Figure 5, Table 1). Across a sample set of 30 reference devices and 23 devices with protrusions, FF increased from 0.55 ± 0.02 to 0.65 ± 0.03, J_{sc} increased from 4.8 ± 0.03 mA cm^{-2} to 5.5 ± 0.03 mA cm^{-2}, and V_{oc} increased from 0.54 ± 0.01 V to 0.59 ± 0.01 V. The absence of any change in the shape of the external quantum efficiency spectrum across the entire visible spectrum (Figure S7, Supporting Information), combined with the significant increase in V_{oc}, indicates that plasmonic effects are not the origin of this improvement in device performance.[49,50]

Incorporation of nanoscale protrusions at the electrode surface increased the electrode surface area by

TABLE 1. OPV Performance Parameters for Devices Employing Ultrathin Au Window Electrodes with Different Nanoscale Protrusion Densities[a]

device type	J_{sc} (mA cm^{-2})	V_{oc} (V)	FF	η (%)	R_s (Ω cm^2)
0 protrusions μm^{-2}	4.8 ± 0.3	0.54 ± 0.01	0.55 ± 0.02	1.4	4.4 ± 2.7
~720 protrusions μm^{-2} (average)	5.5 ± 0.3	0.59 ± 0.01	0.65 ± 0.03	2.1	2.3 ± 0.4
~720 protrusions μm^{-2} (best)	5.6	0.60	0.69	2.3	
~1250 protrusions μm^{-2} (average)	4.8 ± 0.2	0.59 ± 0.01	0.64 ± 0.01	1.8	4.7 ± 1.1

[a] Across a sample set of 30 reference devices and 23 devices with ~720 protrusions μm^{-2}, FF increased from 0.55 ± 0.02 to 0.65 ± 0.03, J_{sc} increased from 4.8 ± 0.03 mA cm^{-2} to 5.5 ± 0.03 mA cm^{-2}, and V_{oc} increased from 0.54 ± 0.01 V to 0.59 ± 0.01 V. At a higher number density of protrusions clustering becomes increasingly prevalent. Ten devices with ~1250 protrusions μm^{-2} were tested.

~25%. To investigate the possibility that this increase in area is responsible for the improvement in OPV performance, the protrusion density was increased by a factor of 1.75 from an average of ~720 protrusions μm^{-2} to ~1250 μm^{-2} such that the surface area was increased by ~60% as compared to the electrode without protrusions. The impact on device performance of this further increase in electrode surface area is a reduction in J_{sc} from 5.5 ± 0.03 to 4.8 ± 0.02 with no change in V_{oc} or FF (Table 1), ruling out the possibility that the improvement in performance observed with the lower density of protrusions results from an increase in the electrode surface area. Furthermore, the reduction in J_{sc} with increasing nanoprotrusion density cannot be rationalized in terms of plasmonic or scattering effects, which, if significant, would result in a photocurrent that scaled with nanoprotrusion number density due to increased light absorption.[51] The sensitivity of OPV performance to the protrusion density is however entirely consistent with GEFE effects, since increasing the number density of protrusions reduces the average separation such that *F* screening begins to erode GEFE at the apex of each protrusion. Indeed, due to the electrode fabrication method used, at a protrusion density of ~1250 μm^{-2} there is an increased prevalence of small clusters of protrusions (Figure S.8, Supporting Information).

The dark current characteristics of OPVs with and without protrusions provide further evidence that GEFE effects are operative. According to the Shockley equation V_{oc} is a logarithmic function of the ratio of J_{sc} to the reverse saturation current, and so achieving the maximum V_{oc} requires the latter to be minimized.[52] However, in this case the increase in V_{oc} is accompanied by a dramatic increase in the reverse dark current by 2 orders of magnitude, which runs contrary to the Shockley model. This observation is entirely consistent with GEFE effects, since under reverse bias in the dark the only source of current is electrons injected from the Au electrode Fermi level into the LUMO of the P3HT layer and holes injected from the Al electrode Fermi level into the HOMO of PCBM. At both of these interfaces the Schottky barrier height to injection is very large (≫1 eV), which gives rise to the diodic *J*−*V* characteristic. However, GEFE at the surface of nanoscale protrusions will operate to enhance *F* regardless of the direction of *F*, thereby increasing the reverse saturation current as compared to the same device employing planar electrodes, as is observed to be the case. Another signature of GEFE effects in the dark *J*−*V* characteristic is the sharp knee in the forward current, which is observed only in devices employing window electrodes with protrusions. This feature is characteristic of GEFE effects[8,53] which would operate to facilitate hole extraction for *V* less than the built-in field (V_{bi}) before abruptly switching to enhance hole injection for $V > V_{bi}$. Further indirect evidence that GEFE effects are responsible for the large improvement in device performance is provided by the device characteristics under 1 sun illumination. In BHJ OPV both donor and acceptor phases are in electrical contact with the hole-extracting electrode, and so there is a significant possibility that free electrons in the PCBM phase are extracted by the *wrong* electrode when *F* is small. This reverse current operates to reduce V_{oc}[17] and can be blocked by incorporating a carrier-selective blocking interfacial layer.[54] Since GEFE at the hole-extracting electrode amplifies *F* in this critical interfacial region, it operates to drive photogenerated electrons away from the contact, consistent with the observed increase in V_{oc} and FF.

Collectively these findings show that GEFE at nanoscale protrusions on the electrode surfaces in organic photovoltaic devices can be harnessed to greatly enhance the efficiency of charge transport across the electrode−organic semiconductor interfaces, while simultaneously improving charge carrier selectivity. The power of this wholly geometric approach to electrode engineering is that it is entirely materials generic and can be employed in a range of organic electronic devices. Compelling evidence of the importance of GEFE at the nanoscale also provides further impetus to the burgeoning field of nanoimprinting, which offers a path to the fabrication of large-area electrodes decorated with nanoscale protrusions for applications.

METHODS

Electrode Design and Fabrication. Glass microscope slides (Menzel-Gläser) were cleaned using a four-stage ultrasonic bath procedure: (i) acetone; (ii) Decon-Neutracon/H_2O; (iii) H_2O; and finally (iv) propan-2-ol. Solvent residue was removed by UV/O_3 treatment before transfer to a desiccator,

where substrates were exposed to MPTMS (Sigma Aldrich) vapor at 5 mbar for 20 h.

The MPTMS-functionalized glass substrates were submerged in toluene solutions with and without Au nanoparticles. The surface density of nanoparticles was controlled by varying the dipping time. The nanoparticle-decorated substrates were then rinsed with toluene, and the OAm capping ligand was exchanged with 1,5-pentanedithiol by submerging in a dilute ethanol solution of the latter for 18 h, followed by rinsing with ethanol. Substrates were then transferred to a vacuum system ($\sim 5 \times 10^{-6}$ mbar) for evaporation of a 9 nm Au film. Immediately prior to device fabrication the Au electrodes were UV/O_3 treated using a Novascan PSD-UVT unit. This process involves exposure of the substrates to UV light from a Hg lamp (185 and 254 nm, 20 mW/cm^2) at a distance of 25 mm from the substrate in a closed air-filled chamber followed by a 15 min incubation period.

P3HT:PCBM OPV Fabrication and Characterization. Filtered blends (PTFE 0.22 μm) of P3HT (Rieke Metals Inc.) and PCBM (Solenne) were spin-cast onto Au electrodes under a nitrogen atmosphere from anhydrous 1,2-dichlorobenzene solutions (1:1 by weight, 20 mg mL^{-1}:20 mg mL^{-1}). The P3HT and PCBM were blended together at 40 °C for three days prior to filtering. Spun films (1000 rpm, 90 s) were allowed to dry at room temperature for 45 min, then annealed at 120 °C for 10 min under an inert atmosphere, before transfer to the vacuum chamber for deposition of 8 nm of bathocuproine (Alfa Aesar) and ~100 nm Al. The photoactive area of devices was defined using a shadow mask to be 6 mm^2.

Device testing was performed in the dark and under AM 1.5 (100 mW cm^2) simulator solar illumination. The light intensity was calibrated using a PV Measurements Inc. calibrated silicon diode with KG5 color filter.

P3HT Diode Fabrication and Characterization. P3HT solutions (20 mg mL^{-1}, 1,2-dichlorobenzene) were processed using the same procedure as for OPV device fabrication. The annealed polymer films were then transferred into the vacuum chamber for deposition of 6 mm^2 Al electrodes through a shadow mask. *J*–*V* measurements were undertaken in the dark at 298 K.

Contact Potential Difference (Kelvin Probe) Measurements. Work function measurements were performed using a Kelvin probe in a nitrogen-filled glovebox and referenced to freshly cleaved HOPG.

Sheet Resistance Measurements. Sheet resistance measurements were made using the 4-point probe Van der Pauw method on square substrates with an applied current of 1 mA.

Scanning Electron Microscopy (SEM). SEM images were made using a ZEISS-SUPRA 55VP operating with an accelerating voltage of 20 kV.

Transmission Electron Microscopy (TEM). The size and shape distribution of the Au nanoparticles were determined using a JEOL 2000FX TEM fitted with a GATAN ORIUS digital camera. Dilute solutions were drop-cast onto lacey carbon Cu (400 mesh) grids for imaging.

Atomic Force Microscopy (AFM). Topography images were obtained using an MFP-3D System (Asylum Research) operating in ac (noncontact) mode. Surface potential measurements were obtained using a Veeco Multimode AFM with Nanoscope V controller in electrical surface potential mode using Ir-coated noncontact mode AFM tips.

Optical Transparency Measurement. Far-field transmittance measurements of Au electrode electrodes on glass were made using a Perkin-Elmer Lambda 25 UV spectrometer over the wavelength range 400–750 nm. The incident beam passed through the glass first, as is the case in OPVs.

Conflict of Interest: The authors declare no competing financial interest.

Acknowledgment. This work was supported by the UK Engineering and Physical Sciences Research Council (EPSRC) and the European Regional Development Agency/Advantage West Midlands Science City Materials Initiative (Project 2). R.A.H. is grateful to the Royal Academy of Engineering/EPSRC for the award of a Fellowship. We thank Ms. Emily Smith (University of Nottingham) for assistance with the XPS data collection and analysis. We also thank Professor Alessandro Troisi, University of Warwick, for his helpful comments.

Supporting Information Available: Electrode characterization and the mathematical model used to calculate the *J*/*V* plots in Figure 4. This information is available free of charge via the Internet at http://pubs.acs.org.

REFERENCES AND NOTES

1. Brabec, C. J.; Gowrisanker, S.; Halls, J. J. M.; Laird, D.; Jia, S.; Williams, S. P. Polymer-Fullerene Bulk-Heterojunction Solar Cells. *Adv. Mater.* **2010**, *22*, 3839–3856.
2. Kippelen, B.; Brédas, J.-L. Organic Photovoltaics. *Energy Environ. Sci.* **2009**, *2*, 251–261.
3. Krebs, F. C.; Nielsen, T. D.; Fyenbo, J.; Wadstrøm, M.; Pedersen, M. S. Manufacture, Integration and Demonstration of Polymer Solar Cells in a Lamp for the "Lighting Africa" Initiative. *Energy Environ. Sci.* **2010**, *3*, 512–525.
4. Forrest, S. R. The Path to Ubiquitous and Low-Cost Organic Electronic Appliances on Plastic. *Nature* **2004**, *428*, 911–918.
5. Li, S.-S.; Tu, K.-H.; Lin, C.-C.; Chen, C.-W.; Chhowalla, M. Solution-Processable Graphene Oxide as an Efficient Hole Transport Layer in Polymer Solar Cells. *ACS Nano* **2010**, *4*, 3169–74.
6. Lee, J. Y.; Connor, S. T.; Cui, Y.; Peumans, P. Solution-Processed Metal Nanowire Mesh Transparent Electrodes. *Nano Lett.* **2008**, *8*, 689–692.
7. Wu, H.; Hu, L.; Rowell, M. W.; Kong, D.; Cha, J. J.; McDonough, J. R.; Zhu, J.; Yang, Y.; McGehee, M. D.; Cui, Y. Electrospun Metal Nanofiber Webs as High-Performance Transparent Electrode. *Nano Lett.* **2010**, *10*, 4242–4228.
8. Pegg, L.-J.; Schumann, S.; Hatton, R. A. Enhancing the Open-Circuit Voltage of Molecular Photovoltaics Using Oxidized Au Nanocrystals. *ACS Nano* **2010**, *4*, 5671–5678.
9. Riede, M.; Mueller, T.; Tress, W.; Schueppel, R.; Leo, K. Small-Molecule Solar Cells—Status and Perspectives. *Nanotechnology* **2008**, *19*, 424001.
10. Steim, R.; Kogler, F. R.; Brabec, C. J. Interface Materials for Organic Solar Cells. *J. Mater. Chem.* **2010**, *20*, 2499–2512.
11. Chen, L.-M.; Xu, Z.; Hong, Z.; Yang, Y. Interface Investigation and Engineering—Achieving High Performance Polymer Photovoltaic Devices. *J. Mater. Chem.* **2010**, *20*, 2575–2598.
12. Potscavage, W. J.; Sharma, A.; Kippelen, B. Critical Interfaces in Organic Solar Cells and Their Influence on the Open-Circuit Voltage. *Acc. Chem. Res.* **2009**, *42*, 1758–1767.
13. Khodabakhsh, S.; Sanderson, B. M.; Nelson, J.; Jones, T. S. Using Self-Assembling Dipole Molecules to Improve Charge Collection in Molecular Solar Cells. *Adv. Funct. Mater.* **2006**, *16*, 95–100.
14. Cook, R. M.; Pegg, L.-J.; Kinnear, S. L.; Hutter, O. S.; Morris, R. J. H.; Hatton, R. A. An Electrode Design Rule for Organic Photovoltaics Elucidated Using Molecular Nanolayers. *Adv. Energy Mater.* **2011**, *1*, 440–447.
15. Ishii, B. H.; Sugiyama, K.; Ito, E.; Seki, K. Energy Level Alignment and Interfacial Electronic Structures at Organic/Metal and Organic/Organic Interfaces. *Adv. Mater.* **1999**, *11*, 605–625.
16. Braun, S.; Salaneck, W. R.; Fahlman, M. Energy-Level Alignment at Organic/Metal and Organic/Organic Interfaces. *Adv. Mater.* **2009**, *21*, 1450–1472.
17. Yuan, Y.; Reece, T. J.; Sharma, P.; Poddar, S.; Ducharme, S.; Gruverman, A.; Yang, Y.; Huang, J. Efficiency Enhancement in Organic Solar Cells with Ferroelectric Polymers. *Nat. Mater.* **2011**, *10*, 296–302.
18. Moliton, A.; Nunzi, J.-M. How to Model the Behaviour of Organic Photovoltaic Cells. *Polym. Int.* **2006**, *55*, 583–600.
19. Jeong, W.-I.; Lee, J.; Park, S.-Y.; Kang, J.-W.; Kim, J.-J. Reduction of Collection Efficiency of Charge Carriers with Increasing Cell Size in Polymer Bulk Heterojunction Solar Cells. *Adv. Funct. Mater.* **2011**, *21*, 343–347.

20. Miller, A. J.; Hatton, R. A.; Silva, S. R. P. Interpenetrating Multiwall Carbon Nanotube Electrodes for Organic Solar Cells. *Appl. Phys. Lett.* **2006**, *89*, 133117.
21. Liu, D.; Fina, M.; Guo, J.; Chen, X.; Liu, G.; Johnson, S. G.; Mao, S. S. Organic Light-Emitting Diodes with Carbon Nanotube Cathode-Organic Interface Layer. *Appl. Phys. Lett.* **2009**, *94*, 013110.
22. Li, L.; Hu, W.; Fuchs, H.; Chi, L. Controlling Molecular Packing for Charge Transport in Organic Thin Films. *Adv. Energy Mater.* **2011**, *1*, 188–193.
23. Kim, J. S.; Granström, M.; Friend, R. H.; Johansson, N.; Salaneck, W. R.; Daik, R.; Feast, W. J.; Cacialli, F. Indium−Tin Oxide Treatments for Single- and Double-Layer Polymeric Light-Emitting Dodes: The Relation between the Anode Physical, Chemical, and Morphological Properties and the Device Performance. *J. Appl. Phys.* **1998**, *84*, 6859–6870.
24. Forbes, R. G.; Edgcombe, C. J.; Valdrè, U. Some Comments on Models for Field Enhancement. *Ultramicroscopy* **2003**, *95*, 57–65.
25. Smith, R. C.; Cox, D. C.; Silva, S. R. P. Electron Field Emission from a Single Carbon Nanotube: Effects of Anode Location. *Appl. Phys. Lett.* **2005**, *87*, 103112.
26. Smith, R. C.; Carey, J. D.; Forrest, R. D.; Silva, S. R. P. Effect of Aspect Ratio and Anode Location on the Field Emission Properties of a Single Tip Based Emitter. *J. Vac. Sci. Technol. B* **2005**, *23*, 632–635.
27. Smith, R. C.; Silva, S. R. P. Interpretation of the Field Enhancement Factor for Electron Emission from Carbon Nanotubes. *J. Appl. Phys.* **2009**, *106*, 014314.
28. Fowler, R. H.; Nordheim, L. Electron Emission in Intense Electric Fields. *Proc. R. Soc. A* **1928**, *119*, 173–181.
29. Li, G.; Shrotriya, V.; Huang, J.; Yao, Y.; Moriarty, T.; Emery, K.; Yang, Y. High-Efficiency Solution Processable Polymer Photovoltaic Cells by Self-Organization of Polymer Blends. *Nat. Mater.* **2005**, *4*, 864–868.
30. Nilsson, L.; Groening, O.; Emmenegger, C.; Kuettel, O.; Schaller, E.; Schlapbach, L.; Kind, H.; Bonard, J.-M.; Kern, K. Scanning Field Emission from Patterned Carbon Nanotube Films. *Appl. Phys. Lett.* **2000**, *76*, 2071–2073.
31. Goss, C. A.; Charych, D. H.; Majda, M. Application of (3-Mercaptopropyl)trimethoxysilane as a Molecular Adhesive in the Fabrication of Vapor-Deposited Gold Electrodes on Glass Substrates. *Anal. Chem.* **1991**, *63*, 85–88.
32. Dunaway, D. J.; McCarley, R. L. Scanning Force Microscopy Studies of Enhanced Metal Nucleation−Au Vapor-Deposited on Self-Assembled Monoloyaers of Substituted Silanes. *Langmuir* **1994**, *10*, 3598–3606.
33. Hatton, R. A.; Willis, M. R.; Chesters, M. A.; Briggs, D. A Robust Ultrathin, Transparent Gold Electrode Tailored for Hole Injection into Organic Light-Emitting Diodes. *J. Mater. Chem.* **2003**, *13*, 722–726.
34. Stec, H. M.; Williams, R. J.; Jones, T. S.; Hatton, R. A. Ultra-Thin Transparent Au Electrodes for Organic Photovoltaics Fabricated Using a Mixed Mono-Molecular Nucleation Layer. *Adv. Funct. Mater.* **2011**, *21*, 1709–1716.
35. Rentenberger, S.; Vollmer, A.; Zojer, E.; Schennach, R.; Koch, N. UV/Ozone Treated Au for Air-Stable, Low Hole Injection Barrier Electrodes in Organic Electronics. *J. Appl. Phys.* **2006**, *100*, 053701.
36. Michaelson, H. B. The Work Function of the Elements and its Periodicity. *J. Appl. Phys.* **1977**, *48*, 4729–4733.
37. Davis, R. J.; Lloyd, M. T.; Ferreira, S. R.; Bruzek, M. J.; Watkins, S. E.; Lindell, L.; Sehati, P.; Fahlman, M.; Anthony, J. E.; Hsu, J. W. P. Determination of Energy Level Alignment at Interfaces of Hybrid and Organic Solar Cells Under Ambient Environment. *J. Mater. Chem.* **2011**, *21*, 1721–1729.
38. Chiatzun, G.; Kline, R. J.; McGehee, M. D.; Kadnikova, E. N.; Frechet, J. M. Molecular-Weight-Dependent Mobilities in Regioregular Poly(3-Hexyl-Thiophene) Diodes. *Appl. Phys. Lett.* **2005**, *86*, 122110.
39. Helander, M. G.; Wang, Z. B.; Greiner, M. T.; Qiu, J.; Lu, Z. H. Experimental Design for the Determiniation of the Injection Barrier Height at Metal/Organic Interfaces using Temperature Dependent Current-Voltage Measurements. *Rev. Sci. Instrum.* **2009**, *80*, 033901.
40. Dennler, G.; Sariciftci, N. S.; Schwödiauer, R.; Bauer, S.; Reiss, H. Unexpected Electromechanical Actuation in Conjugated Polymer Based Diodes. *J. Mater. Chem.* **2006**, *16*, 1789–1793.
41. Shen, Y.; Hosseini, A. R.; Wong, M. H.; Malliaras, G. G. How to Make Ohmic Contacts to Organic Semiconductors. *ChemPhysChem.* **2004**, *5*, 16–25.
42. Lambert, M. A., Mark, P. *Current Injection in Solids*; Academic Press: New York, 1970.
43. Davids, P. S.; Parker, I. D.; Smith, D. L. Charge Injection in Organic Light-Emitting Diodes: Tunneling into Low Mobility Materials. *Appl. Phys. Lett.* **1996**, *69*, 2270–2272.
44. Yang, G.; Chin, K. K.; Marcus, R. B. Electron Field Emission through a Very Thin Oxide Layer. *IEEE Trans. Electron Devices* **1991**, *38*, 2373–2376.
45. Tremolet de Villers, B.; Tassone, C. J.; Tolbert, S. H.; Schwartz, B. J. Improving the Reproducibility of P3HT:PCBM Solar Cells by Controlling the PCBM/Cathode Interface. *J. Phys. Chem. C* **2009**, *113*, 18978–18982.
46. Kim, Y.; Cook, S.; Tuladhar, S. M.; Choulis, S. A; Nelson, J.; Durrant, J. R.; Bradley, D. D. C.; Giles, M.; McCulloch, I.; Ha, C.-S.; Ree, M. A Strong Regioregularity Effect in Self-Organizing Conjugated Polymer Films and High-Efficiency Polythiophene:Fullerene Solar Cells. *Nat. Mater.* **2006**, *5*, 197–203.
47. Clark, J.; Chang, J.-F.; Spano, F. C.; Friend, R. H.; Silva, C. Determining Exciton Bandwidth and Film Microstructure in Polythiophene Films Using Linear Absorption Spectroscopy. *Appl. Phys. Lett.* **2009**, *94*, 163306.
48. Reid, O. G.; Nekuda Mailk, J. A.; Latini, G.; Dayal, S.; Kopidakis, N.; Silva, C.; Stingelin, N.; Rumbles, G. The Influence of Solid-State Microstructure on the Origin and Yield of Long-Lived Photogenerated Charge in Neat Semiconducting Polymers. *J. Polym. Sci. B: Polym. Phys.* **2012**, *50*, 27–37.
49. Reilly, T. H.; Lagemaat, J.; van de, Tenent, R. C.; Morfa, A. J.; Rowlen, K. L. Surface-Plasmon Enhanced Transparent Electrodes in Organic Photovoltaics. *Appl. Phys. Lett.* **2008**, *92*, 243304.
50. Wu, J.-L.; Chen, F.-C.; Hsiao, Y.-S.; Chien, F.-C.; Chen, P.; Kuo, C.-H.; Huang, M. H.; Hsu, C.-S. Surface Plasmonic Effects of Metallic Nanoparticles on the Performance of Polymer Bulk Heterojunction Solar Cells. *ACS Nano* **2011**, *5*, 959–967.
51. Kulkarni, A. P.; Noone, K. M.; Munechika, K.; Guyer, S. R.; Ginger, D. S. Plasmon-Enhanced Charge Generation in Organic Photovoltaic Films Using Silver Nanoprisms. *Nano Lett.* **2010**, *10*, 1501–1505.
52. Brumbach, M.; Placencia, D.; Armstrong, N. R. Titanyl Phthalocyanine/C_{60} Heterojunctions: Band-Edge Offsets and Photovoltaic Device Performance. *J. Phys. Chem. C* **2008**, *112*, 3142–3151.
53. Xie, X. N.; Gao, X.; Qi, D.; Xie, Y.; Shen, L.; Yang, S.-W.; Sow, C. H.; Thye, A.; Wee, S. Chemically Linked AuNP-Alkane Network for Enhanced Photoemission and Field Emission. *ACS Nano* **2009**, *3*, 2722–2730.
54. Peumans, P.; Forrest, S. R. Very-High-Efficiency Double-Heterostructure Copper Phthalocyanine/C_{60} Photovoltaic Cells. *Appl. Phys. Lett.* **2001**, *79*, 126–128.